Volume 1 | Number 1 | Jan 2013 | Pages 1–100

RSC Advances

www.rsc.org/advances

Incorporation of SnO$_2$ nanoparticles in PMMA for performance enhancement of transparent organic resistive memory device

Pranab Kumar Sarkar, [1] Snigdha Bhattacharjee[1], Manoj Prajapat[2] and Asim Roy[1*]

[1]*Department of Physics*
National Institute of Technology Silchar
Silchar-788010, Assam, India
email:28.asim@gmail.com
[2]*Department of Physics*
Indian Institute of Science Education and Research (IISER) Bhopal
Bhopal – 462066, Madhya Pradesh, India

We report the electrical bistable characteristics of a hybrid polymer/inorganic nanocomposites device consisting of SnO$_2$ nanoparticles (NPs) embedded in an insulating polymethylmethacrylate (PMMA) layer sandwiched between a conductive indium tin oxide (ITO) and aluminium (Al) electrodes. X-ray diffraction measurements were performed for assessment of crystallographic nature of SnO$_2$ nanoparticles while microstructural nature of SnO$_2$ nanoparticles embedded in PMMA matrix was confirmed using transmission electron microscopy. A detailed electrical characterizations suggested an influence of the NPs concentration on switching characteristic of the Al/ SnO$_2$-PMMA/ITO memory devices. Highest resistance ratio > 10^3 (R$_{off}$/R$_{on}$) was observed in a device with 2 weight % SnO$_2$ NPs. The retention tests on fabricated device demonstrated the consistency in current of ON/OFF state even after 10^4 s. The conduction mechanisms of the fabricated nanocomposite based memory cell were discussed on the basis of experimental data using charge trapping-detrapping mechanism in NPs. Our findings offer a feasible and low cost chemical approach to fabricate a transparent and high density RS memory device.

Keywords: Organic memory devices; Resistive memory; SnO$_2$ nanoparticles; Conduction mechanism

1

1. Introduction

Resistive random access memory (RRAM)[1-6] have emerged as a promising candidate for future non-volatile memory (NVM) application facilities with continuing miniaturization of data memory storage, low power operation and long retention performance. Among various NVMs,[7-9] RRAM have a potential to be supplementary of conventional NAND flash and dynamic random access memories (DRAM) based memory technologies due to the advantages of small size, long retention time and large capacity for data storage[8]. Organic[10-15], inorganic[16] and hybrid inorganic/organic composites[17-19] are widely used as switching materials. Organic materials and polymer nanocomposites containing inorganic nanoparticles (NPs)[20, 21] have extensive advantages over inorganic materials due to their ease scalability, simple processability onto a range of substrates with variety of shape,[22] flexibility with good mechanical strengths,[12, 23, 24] low costing and high transparency.[25] Therefore, organic bistable devices (OBDs) have become highly attracting for their potential applications in future organic based resistive switching (RS) devices. Some fundamental investigations about the RS mechanisms in OBDs using the synthesized inorganic nanoparticles blended in the insulating organic layer have been studied.[26-30] Carrier transport mechanism in OBDs utilizing hybrid organic/inorganic nanocomposites have been explained typically by space-charge-limited-current (SCLC),[10, 13, 19, 29, 31-34] ionic conduction,[35] Ohmic conduction,[10, 12, 18, 20] hopping conduction[36] and Fowler-Nordheim (FN) tunnelling,[37, 38] including thermionic emission (TE).[11, 12, 18] Furthermore, a systematic study on the RS mechanisms and switching parameters (Current ON/OFF ratio, SET/RESET voltage, endurance and retention time) are needed to enhance device efficiency.

In this paper, we report on the fabrication of OBDs with Al/SnO_2-PMMA/ITO structure at different concentrations of SnO_2 NPs by using a simple spin-coating method. The 2 wt% SnO_2 NPs embedded OBD exhibits good optical-transparency of $\approx 80\%$ in the visible

region with a high on/off ratio of 10^3, high cell-to-cell uniformity and long term stability. Based on the experimental observations, the electrical properties of the as-fabricated devices are systematically investigated and a model for the switching phenomena is demonstrated. The present SnO_2 NPs embedded devices are of great potential for future transparent electronic applications.

2. Experimental details

Stannic chloride pentahydrate ($SnCl_4$, $5H_2O$) was used as a source to synthesize SnO_2 NPs. In the first step, 4.2452 g of $SnCl_4$, $5H_2O$ was added to 80 ml of methanol and the solution was vigorously stirred at 50 ℃ for 70 min, leading to the formation of gel. Then the products were rinsed with deionized water, air dried and annealed at 250 ℃ for 1 h in air to obtain nanocrystalline SnO_2 powder. The PMMA polymer was dissolved in chloroform with concentration of 4 weight (wt) %. Subsequently, the synthesized SnO_2 NPs were added to the PMMA solution with concentrations of 0.5, 1, 2, 3 wt % and the mixed solution was ultrasonicated for 30 min. Prior to deposition, ITO coated glass substrates were ultrasonically cleaned in acetone, methanol for 15 min subsequently and were thoroughly rinsed in deionized water. A 110 nm thick SnO_2 NPs- PMMA layer was deposited on patterned ITO coated glass substrate by spin-coating at 2000 rpm for 60 s and then dried in an oven at 85 ℃ for 10 min. As a top electrode (TE), a 200 nm thick Al was thermally evaporated using shadow mask of area 0.18 mm^2. A 200 keV JEM – 2100 transmission electron microscope (TEM) was used to study the microstructural nature of SnO_2 NPs and SnO_2 blended PMMA layer deposited on Si substrate. Phase structures of the SnO_2 NPs nanoparticles were investigated using PANalytical Empyrean X-ray diffractometer equipped with Cu K_α radiation (λ = 1.54 Å). Current-voltage (I-V) characteristics of Al/SnO_2 NPs- PMMA/ ITO devices were performed by using Keithley 4200 SCS. All the electrical measurements of memory devices were performed at room temperature (RT). Figure 1 shows the schematic

diagram of transparent memory device with transmittance data for 2 wt % SnO_2-PMMA nanocomposite.

3. Results and Discussion

Figure 2 shows the XRD pattern for the SnO_2 NPs annealed at 250 °C. All the diffraction peaks of SnO_2 NPs are well indexed to the tetragonal phase of SnO_2, according to the reported JCPDS No. 77-0449 card. The average crystallite size (D) of SnO_2 NPs is calculated using the following equation[39]

$$D = k\lambda/\beta\cos\theta \qquad (1)$$

where, D is the crystallite size, assuming particles to be spherical k = 0.94, λ is the wavelength of X-ray, β is the full width at half maximum of the diffracted peak and θ is the Bragg angle of diffraction peaks. The average crystallite size is estimated to be 18 nm.

Figure 3(a) shows the TEM image of several SnO_2 NPs and inset figure represents the histogram of the NP diameter distribution. The size of the SnO_2 NPs is approximately 14 nm. Figure 3(b) shows the cross sectional TEM image of 2 wt % SnO_2 NPs - PMMA layer. A high-resolution TEM (HRTEM) image (inset of Fig. 3 b) establishes arbitrary distribution of the SnO_2 NPs in the PMMA layer which may affect the electrical performance of the memory device. Energy dispersive spectroscopy (EDS) analyses reveal that the constituent elements of the NPs are Sn and O_2, as shown in figure 3(c). Figure 3(d) illustrates the selected area electron diffraction (SAED) pattern of aggregated NPs, whose diffraction rings from outside to inside can be indexed as (211), (200), (101) and (110) planes of rutile phase SnO_2, respectively.

To analyze the switching performance, the dc *I–V* characteristics of SnO_2 NPs embedded devices have been studied. Figure 4(a) distinctively displays bipolar resistive switching (BRS) characteristics in Al/SnO_2-PMMA/ITO memory cells with concentrations of SnO_2 NPs 0.5, 1, 2 and 3 wt %. The arrows in Fig. 4 indicate the voltage sweep direction. For

the Al/SnO$_2$ (2 wt %)-PMMA/ITO device, starting with the high resistance state (HRS) the current increased slowly with the applied negative voltage (sweep1) and switched to the low resistance state (LRS) at –3.9 V. The LRS can be retained after removing the voltage supply (sweep 2) and switching back (erasing process) to HRS under a positive bias (3.4 V) on TE (sweep 3). Since PMMA acts as an insulating material,[22] the I-V characteristics of Al/SnO$_2$-PMMA/ITO device would be dominated by the number density of SnO$_2$ NPs. Indeed, ON/OFF state currents depend on the wt % of SnO$_2$ NPs, as shown in Fig 4(b). The current in LRS tends to increase with increasing concentration of SnO$_2$ NPs. On the contrary, it has been observed that maximum resistance (R_{off}/R_{on}) ratio is obtained for the device with 2 wt % than that for 3 wt % because of large aggregations of SnO$_2$ NPs inside the insulating layer makes a robust conductive channel between the electrodes under the applied electric field.[22, 26, 40]

In order to know more about the charge transport mechanism for the OBDs with concentration of 2 wt % SnO$_2$ NPs , the (I-V) curve was re-plotted in the log scale [Figure 5 (a, b)]. When a small negative bias voltage was applied to the pristine Al/SnO$_2$-PMMA/ITO device in its initial HRS, Ohmic conduction was observed, as shown in Fig 5 (a).[2, 10, 13, 14, 29, 31] Moreover, (I–V) curve at very low applied bias (0 to -0.45 V) in the HRS could be fitted by using TE process, as shown in inset of Fig. 5(a). This suggests that the charge transport at very low voltage is also governed by the thermal emission of charge carriers over the energy barrier between Al and PMMA when the barrier is not too high for thermal injection.[17] With the increase of electric field from –1.3 V to –2.9 V, the number of injected electrons becomes comparable with the thermally generated free electrons.[29] Therefore, the electronic transport was predominated by injected electrons which are partly trapped at the interface Al/PMMA.[18, 41, 42] As a result the carrier conduction strays significantly from Ohmic conduction, giving rise to space–charge-limited-current (SCLC) conduction behaviour with

5

slope ~ 2, (Fig. 5 a).[10, 12, 13, 18, 31] The results indicate that the captured carriers in SnO_2 NPs

embedded PMMA matrix can act as space charges. The electron mobility value of SnO_2 NPs

blended PMMA thin film is found to be 1.3×10^{-12} m^2/Vs by using the following equation[2]

$$J = \frac{9}{8} \mu \varepsilon \varepsilon_0 \frac{V^2}{d^3} \qquad (2)$$

where J, μ, ε and d are the current density, electron mobility, dielectric constant and

thickness of the thin film, respectively.

With further increase of applied bias up to −3.9 V, steep current flows through the

device with large linear slope value of 4 [Fig. 5 (a)].[10, 14, 19, 31] Interestingly, the SnO_2 NPs are

playing the role as the traps sites which are able to hold the charges very firmly, as proven

from long retention test (Fig 7b).[12, 41] Once all the traps of SnO_2 are completely filled up, the

OBD switch to the LRS. As a result, the LRS conduction regains the Ohmic [Figure 5(a)]

nature with slope ~ 1.[5, 10, 12, 14, 15, 18, 31] Figure 5 (b) shows the similar kind of behaviour in

positive bias region that was observed in case of negative bias condition in the RS devices.

Figure 5(c) shows the capacitance–voltage (C–V) at high frequency (500 kHz) for the SnO_2

NPs embedded OBD. The calculated value of dielectric constant of SnO_2 NPs embedded

PMMA thin film is found to be ~ 6. The large hysteresis in C–V curve indicates that trapping

regulates the memory effect of SnO_2 NPs embedded PMMA device.[43] The charge trapping

density for SnO_2 NPs blended PMMA device is estimated to be 2.1×10^{12} cm^{-2} by using the

following equation[43]

$$N_{electron} = \frac{C \times \Delta V_{FB}}{q \times A} \qquad (3)$$

where C is capacitance, A is electrode area, flat band voltage shift (ΔV_{FB}) and q is the

charge of electron.

To investigate the memory performance of Al/2 wt % SnO_2-PMMA/ITO structure, we

performed a series of characterizations such as statistical distributions of LRS/HRS and SET/

RESET voltage, endurance and retention test. Figure 6(a) shows the distributions of

6

V_{SET}/V_{RESET} for the Al/SnO$_2$-PMMA/ITO OBDs during the device-to-device (D/D) operation. For D/D the mean values (μ) and standard deviations (σ) of V_{SET} and V_{RESET} are – 3.6 V, 3.5 V and 0.37, 0.34, respectively. Small values of σ indicate less spreading in distribution of SET/ RESET voltage which indicates the uniform distribution of SnO$_2$ NPs throughout the PMMA matrix. Figure 6(b) also indicates uniform cumulative distribution of R_{LRS}/R_{HRS} of the hybrid SnO$_2$-PMMA switching devices during the cycle-to-cycle (C/C) and (D/D) operation. The mean values (μ) of R_{LRS} and R_{HRS} are 96 and 69.4 kΩ and 170 and 193 MΩ for (C/C) and (D/D) operation, respectively. Due to high resistance ratio (HRS/LRS > 10^3), the device has potential for use in RS memory application with enhanced data storage capacity. The endurance and retention properties of both 1 and 2 wt % SnO$_2$-NPs embedded memory cells are illustrated in Fig 7. Figure 7(a) represents the repetitive sweeps; this consists of write, erase, and read cycles for the selected cell of 1 and 2 wt % SnO$_2$ NPs blended memory device. During the endurance test, OBDs maintained their HRS/LRS ratios of over~10^3 without showing any substantial electrical degradation. Figure 7(b) shows a good retention property with a rewriting capability over a 10^4 s test period of 1 and 2 wt % SnO$_2$ NPs embedded OBDs.

In order to study the observed memory characteristics, we considered the work function of Al and ITO electrodes[44] and energy gap between the highest occupied molecular orbital (HOMO) and lowest unoccupied molecular orbital (LUMO) of PMMA[44] and the electronic structure of conduction and valence band of SnO$_2$,[45] as shown in figure 8 (a). The energy barrier between the electrodes and the conduction band of SnO$_2$ is smaller than that of the electrodes and the valence band of SnO$_2$.[18, 46] Thus, for both forward and reverse applied bias, electron injection is more favorable over holes injection from the electrode. However, since the barrier between ITO and SnO$_2$ NPs (0.5 eV) is greater than that between Al and SnO$_2$ NPs (0.1 eV), electron injection efficiency from ITO electrode is relatively lower than

that from Al electrode to SnO_2. As a result difference in trapping and detrapping processes are observed under the forward and reverse voltage sweep.[11, 43] The current conduction process in the Al/SnO_2-PMMA/ITO device is mainly governed via charge trapping mechanism by the SnO_2 NPs associated with the filamentary conduction mechanism due to local degradation of PMMA layer.[18, 22, 41, 44, 46] On the basis of the aforesaid discussion, the write/erase operational mechanism of the switching memory device is elucidated in figures 8 (b), (c) and (d). When low electric field is applied to the Al electrode the OFF state current increases with decreasing trap depth. This is because of the low electron occupation probability in the trap with a shallow depth. Therefore, free electron density increases and the HRS current in low voltage (~ –1 V) can be attributed to the Ohmic process. At higher voltage region (–1 V< V < –3 V) the electrons existing at the conduction band of SnO_2 are transported along the direction of the applied electric field by the trapped charge limited current (TCLC) conduction process.[41, 44] The electric field among adjacent SnO_2 NPs increases with the increase of applied voltages.[46] Hence, the SnO_2 NPs act as electron trapping sites due to the lower energy levels of SnO_2 between the PMMA layers and the space charge formation by electron trapping dominates the conduction process.[22, 46] However, the SnO_2 NPs in the HRS are partly occupied as some of the trapped electrons are emitted from the SnO_2 NPs to the ITO electrode, as shown in figure 8 (b).[18, 41] When the applied voltage is very high ($\geq$ –3.9 V) the free electron density is very large due to high injection current. Consequently, the electron occupation probability becomes larger as the Fermi level moves to the LUMO level of PMMA.[47] As a result band bending of PMMA at PMMA/Al interface is much more than that of PMMA/ITO interface. Even though the trap depths are different, all traps under high voltages are completely occupied by electrons, resulting in an increase in film conductivity.[12, 18, 41, 46]. Therefore, SnO_2 embedded PMMA based memory device with different trap depths exhibit the same ON-state current characteristics under high

voltages (-3.9 to − 5 V). As a result device switches from the OFF state to the ON state. This bistable transition is known as writing process for the memory devices, as shown in figure 8(c). The LRS current is attributed to the Ohmic process by trap filled states and filamentary channels by localized degradation of polymer layer.[12, 18, 46] After the applied voltage is withdrawn, the device can remain in the LRS which is indicative of nonvolatile nature of the Al/SnO$_2$-PMMA/ITO device. Subsequently, when a positive voltage is applied to the Al electrode, OBD retains in LRS until the reset voltage of 3.4 V is reached. Nevertheless, at a higher voltage (>3.4 V) the electron captured in the SnO$_2$ NPs are detrapped under reverse electric field, as shown in Fig. 8 (d), and is known as erasing process. Eventually, this causes a significant decrease in the current and the OFF state re-appears in Al/SnO$_2$-PMMA/ITO memory device.[18]

4. Conclusion

In conclusion, OBDs based on hybrid SnO$_2$ NPs-PMMA heterostructures were fabricated using a spin-coating technique. TEM image exhibited a random distribution of SnO$_2$ NPs in the PMMA matrix. The SnO$_2$ NPs-PMMA nanocomposite sandwiched between Al and ITO electrodes, showed very good memory effect. The effective memory property of the non-aggregated SnO$_2$ NPs-PMMA nanocomposite devices was much higher than that of the aggregated SnO$_2$ NPs-PMMA nanocomposite device. The maximum R$_{off}$/R$_{on}$ ratio is obtained for the device with 2 wt % SnO$_2$ NPs in the PMMA polymer. No degradation of current was observed in LRS and HRS after quite a long retention test. The carrier conduction was controlled by the Ohmic, SCLC and TCLC in the HRS and by only Ohmic in the LRS.

References

1. R. Waser and M. Aono, *Nat Mater*, 2007, 6, 833-840.
2. K. M. Kim, B. J. Choi, Y. C. Shin, S. Choi and C. S. Hwang, *Applied Physics Letters*, 2007, 91, 012907.

3. Y.-F. Chang, P.-Y. Chen, B. Fowler, Y.-T. Chen, F. Xue, Y. Wang, F. Zhou and J. C. Lee, *Journal of Applied Physics*, 2012, 112, 123702.

4. Y.-F. Chang, B. Fowler, Y.-C. Chen, Y.-T. Chen, Y. Wang, F. Xue, F. Zhou and J. C. Lee, *Journal of Applied Physics*, 2014, 116, 043709.

5. L.-W. Feng, C.-Y. Chang, Y.-F. Chang, W.-R. Chen, S.-Y. Wang, P.-W. Chiang and T.-C. Chang, *Applied Physics Letters*, 2010, 96, 052111.

6. P. K. Sarkar and A. Roy, *Surface Review and Letters*, 2015, 22, 1550031.

7. S. Tehrani, J. M. Slaughter, E. Chen, M. Durlam, J. Shi and M. DeHerren, *Magnetics, IEEE Transactions on*, 1999, 35, 2814-2819.

8. J. I. Sohn, S. S. Choi, S. M. Morris, J. S. Bendall, H. J. Coles, W.-K. Hong, G. Jo, T. Lee and M. E. Welland, *Nano Letters*, 2010, 10, 4316-4320.

9. S. Hudgens and B. Johnson, *MRS Bulletin*, 2004, 29, 829-832.

10. W. Elsawy, M. Son, J. Jang, M. J. Kim, Y. Ji, T.-W. Kim, H. C. Ko, A. Elbarbary, M.-H. Ham and J.-S. Lee, *ACS Macro Letters*, 2015, 4, 322-326.

11. H. Ye, G. Tian, L. Shi, S. Qi and D. Wu, *European Polymer Journal*, 2015, 63, 45-57.

12. Y. Zhou, S.-T. Han, Y. Yan, L. Zhou, L.-B. Huang, J. Zhuang, P. Sonar and V. A. L. Roy, *Scientific Reports*, 2015, 5, 10683.

13. Y. Sun, L. Li, D. Wen and X. bai, *Organic Electronics*, 2015, 25, 283-288.

14. B.-H. Lee, H. Bae, H. Seong, D.-I. Lee, H. Park, Y. J. Choi, S.-G. Im, S. O. Kim and Y.-K. Choi, *ACS Nano*, 2015, 9, 7306-7313.

15. J. Chen, L. Xu, J. Lin, Y. Geng, L. Wang and D. Ma, *Applied Physics Letters*, 2006, 89, 083514.

16. K. Onlaor, B. Tunhoo, P. Keeratithiwakorn, T. Thiwawong and J. Nukeaw, *Solid-State Electronics*, 2012, 72, 60-66.

17. Y. N. Kim, D. Y. Yun, N. S. Arul and T. W. Kim, *Organic Electronics*, 2015, 17, 270-274.

18. P.-C. Kao, C.-C. Liu and T.-Y. Li, *Organic Electronics*, 2015, 21, 203-209.

19. S. Song, T.-W. Kim, B. Cho, Y. Ji and T. Lee, *Journal of Nanoscience and Nanotechnology*, 2011, 11, 4492-4495.

20. L. Heng-Tien, Z. Pei and Y.-J. Chan, *Electron Device Letters, IEEE*, 2007, 28, 569-571.

21. S. Moller, C. Perlov, W. Jackson, C. Taussig and S. R. Forrest, *Nature*, 2003, 426, 166-169.

22. T. Thanh Dao, T. Viet Tran, K. Higashimine, H. Okada, D. Mott, S. Maenosono and H. Murata, *Applied Physics Letters*, 2011, 99, 233303.

23. S. Song, J. Jang, Y. Ji, S. Park, T.-W. Kim, Y. Song, M.-H. Yoon, H. C. Ko, G.-Y. Jung and T. Lee, *Organic Electronics*, 2013, 14, 2087-2092.

24. T. Sekitani, T. Yokota, U. Zschieschang, H. Klauk, S. Bauer, K. Takeuchi, M. Takamiya, T. Sakurai and T. Someya, *Science*, 2009, 326, 1516-1519.

25. J. C. Scott and L. D. Bozano, *Advanced Materials*, 2007, 19, 1452-1463.

26. S. ChandraKishore and A. Pandurangan, *RSC Advances*, 2014, 4, 9905-9911.

27. U. S. Bhansali, M. A. Khan, D. Cha, M. N. AlMadhoun, R. Li, L. Chen, A. Amassian, I. N. Odeh and H. N. Alshareef, *ACS Nano*, 2013, 7, 10518-10524.

28. S. H. Sung and B. W. Boudouris, *ACS Macro Letters*, 2015, 4, 293-297.

29. D. Y. Yun, N. S. Arul, D. U. Lee, N. H. Lee and T. W. Kim, *Organic Electronics*, 2015, 24, 320-324.

30. T. Lee and Y. Chen, *MRS Bulletin*, 2012, 37, 144-149.

31. J. R. Rani, S.-I. Oh, J. M. Woo and J.-H. Jang, *Carbon*, 2015, 94, 362-368.

32. G. Peng, D. Yuan-Wei, J. Xin, L. Yin-Xiang and X. Wei, *Electron Device Letters, IEEE*, 2007, 28, 572-574.

33. F. Li, D.-I. Son, H.-M. Cha, S.-M. Seo, B.-J. Kim, H.-J. Kim, J.-H. Jung and T. W. Kim, *Applied Physics Letters*, 2007, 90, 222109.

34. J. H. Jung, J.-H. Kim, T. W. Kim, M. S. Song, Y.-H. Kim and S. Jin, *Applied Physics Letters*, 2006, 89, 122110.

35. F. Verbakel, S. C. J. Meskers and R. A. J. Janssen, *Chemistry of Materials*, 2006, 18, 2707-2712.

36. D. Attianese, M. Petrosino, P. Vacca, S. Concilio, P. Iannelli, A. Rubino and S. Bellone, *Electron Device Letters, IEEE*, 2008, 29, 44-46.

37. A. Kanwal and M. Chhowalla, *Applied Physics Letters*, 2006, 89, 203103.

38. J. Ouyang, C.-W. Chu, D. Sieves and Y. Yang, *Applied Physics Letters*, 2005, 86, 123507.

39. R. D. Sakhare, G. D. Khuspe, S. T. Navale, R. N. Mulik, M. A. Chougule, R. C. Pawar, C. S. Lee, S. Sen and V. B. Patil, *Journal of Alloys and Compounds*, 2013, 563, 300-306.

40. D. I. Son, C. H. You, W. T. Kim, J. H. Jung and T. W. Kim, *Applied Physics Letters*, 2009, 94, 132103.

41.   S. Dong-Ick, P. Dong-Hee, C. Won Kook, C. Sung-Hwan, K. Won-Tae and K. Tae Whan, *Nanotechnology*, 2009, 20, 195203.

42.   H. Yoshida and N. Sato, *Applied Physics Letters*, 2007, 91, 141915.

43.   Q. Shi, J. Xu, Y. Wu, Y. Wang, X. Wang, Y. Hong, L. Jiang and L. Li, *Physics Letters A*, 2014, 378, 3544-3548.

44.   D. I. Son, C. H. You, J. H. Jung and T. W. Kim, *Applied Physics Letters*, 2010, 97, 013304.

45.   T. Tharsika, A. Haseeb, S. Akbar, M. Sabri and W. Hoong, *Sensors*, 2014, 14, 14586.

46.   K. Onlaor, T. Thiwawong and B. Tunhoo, *Organic Electronics*, 2014, 15, 1254-1262.

47.   J. H. Jung and T. W. Kim, *Journal of Applied Physics*, 2011, 110, 043721.

Figure Caption

Figure 1. Optical transmittance (UV–visible) spectra of SnO_2 NPs embedded in PMMA matrix. The inset illustrates a schematic diagram of the Al/SnO_2-PMMA/ITO memory devices and chemical structure of polymethylmethacrylate (PMMA).

Figure 2 XRD pattern of SnO_2 NPs.

Figure 3. (a) TEM image of SnO_2 NPs (inset: histogram of the SnO_2 NPs Size distribution) ; (b) cross sectional TEM image of SnO_2 NPs embedded in PMMA matrix (inset: enlarged image of the selected area); (c) EDS spectrum of that layer; (d) SAED pattern of the SnO_2 NPs.

Figure 4. (a) Current-voltage curves for the Al/ SnO_2-PMMA/ITO memory devices with SnO_2 concentrations of 0.5, 1, 2 and 3 wt %. (b) Dependence of HRS current (open square), LRS currents (open circles) and on/off ratio (filled circles) on Weight % of SnO_2 NPs. Read voltage was 0.5 V.

Figure 5. I-V curves of the investigated Al/SnO_2-PMMA/ITO OBDs in log-log scale and Current conduction mechanisms: (a) negative bias region, (b) positive bias region. Insets of Figure (a) and (b) shows the selected experimental data and fitted lines of the I-V characteristics with TE model. (c) Capacitance–Voltage (C-V) curve for the 2 wt % SnO_2 NPs embedded PMMA device.

Figure 6. (a) SET and RESET voltage distributions for the 'write' and the 'erase' processes (b) Cumulative probability data for the resistances of the low-resistance state (LRS) and high-resistance state (HRS) during cycle-to-cycle and device-to-device operation.

Figure 7. (a) Endurance data of both 1and 2 wt % SnO_2 NPs embedded memory devices and (b) Their retention characteristics at room temperature. The device was read with pulse reading bias of -1 V (pulse width: 2µs)

Figure 8. (a) Schematic structure and energy level diagram for the Al/SnO_2-PMMA/ITO device (non-contact state). Schematic diagrams of the charge carrier transport path corresponding to the operating mechanisms for fabricated devices with the (b and c) writing and (d) erase process.
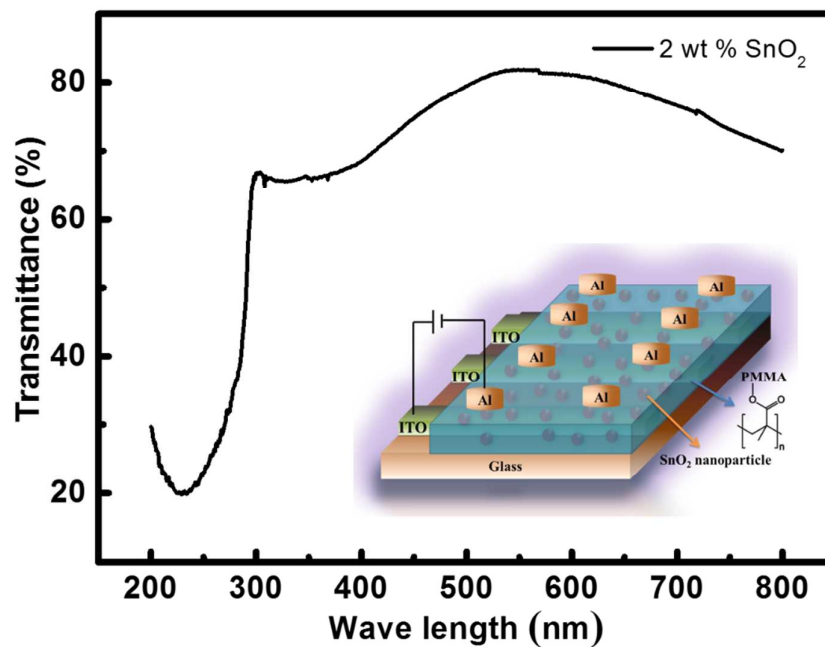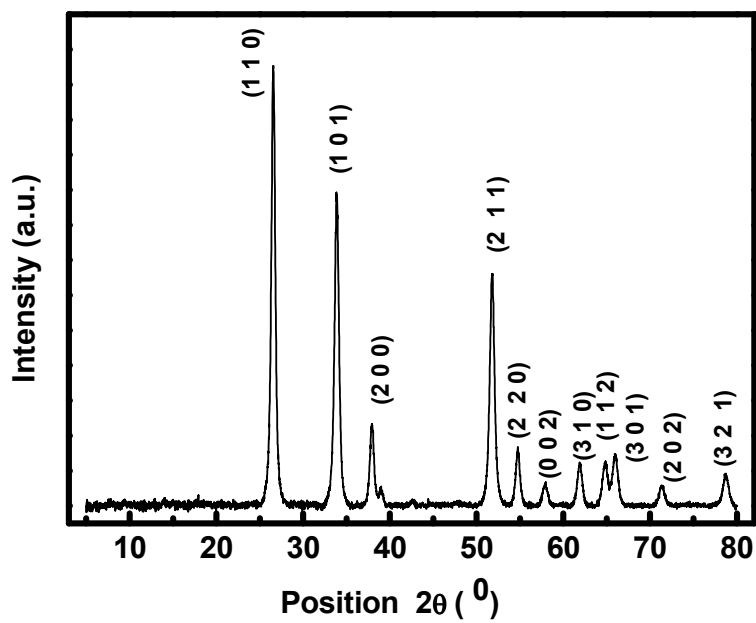
13

Figure 1
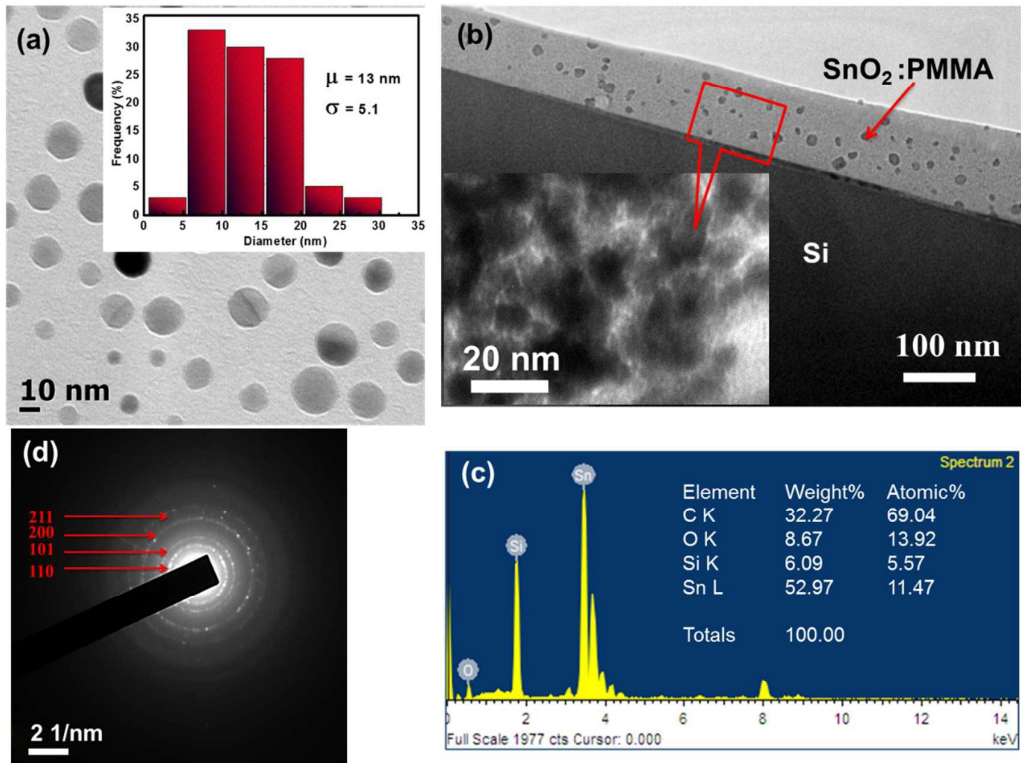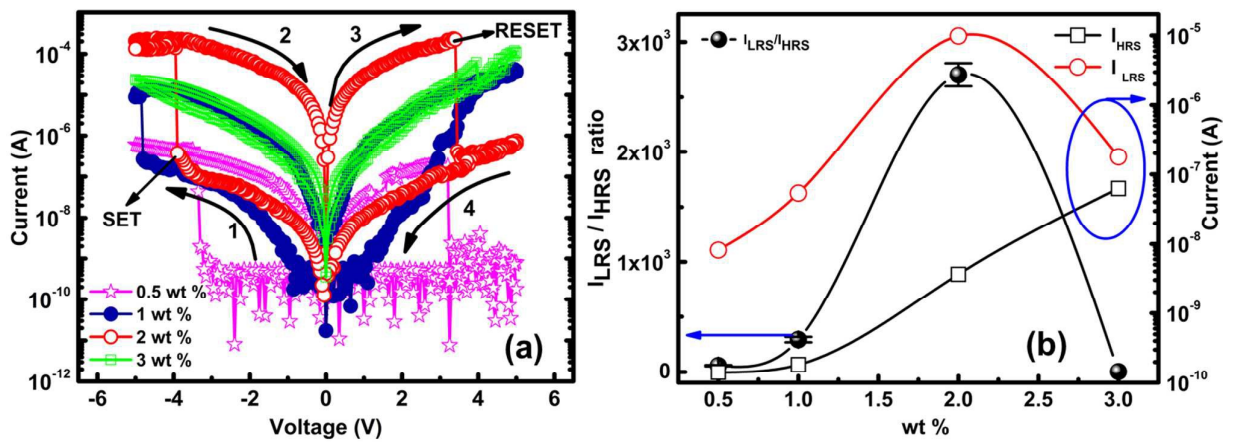P k Sarkar et al.

Figure 2
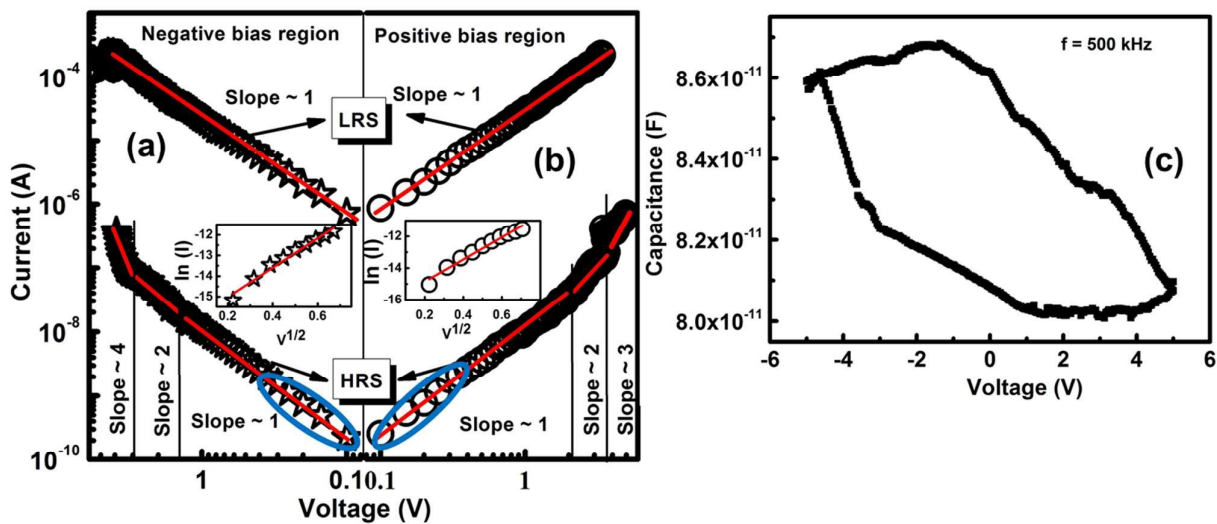P k Sarkar et al.

Figure 3
P k Sarkar et al.

Figure 4
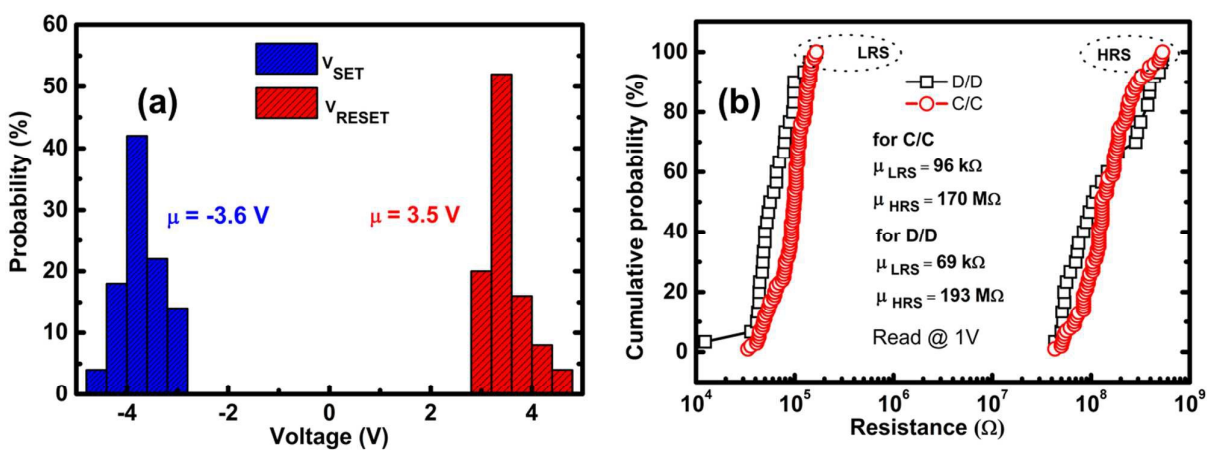P k Sarkar et al.

15

Figure 5
P k Sarkar et al.

Figure 6
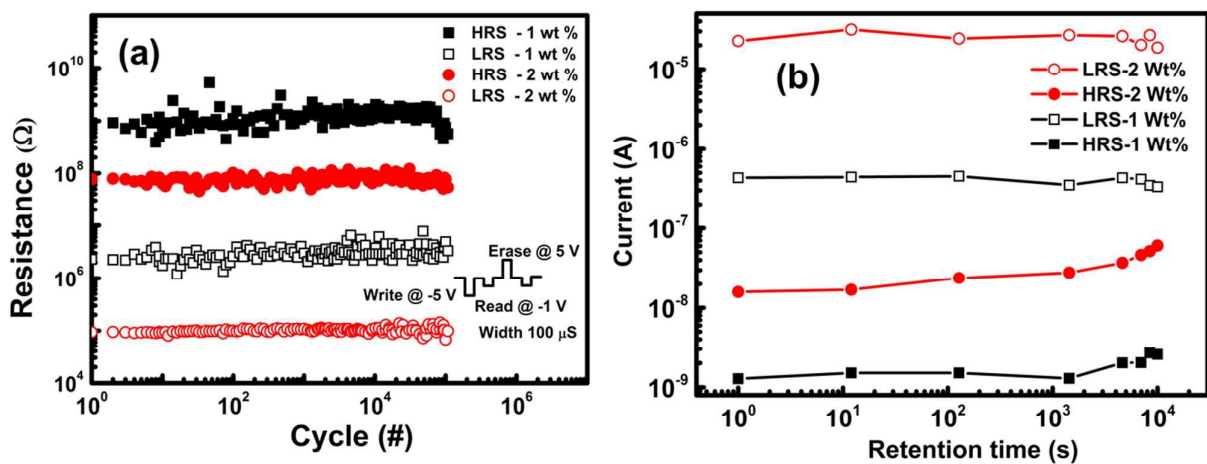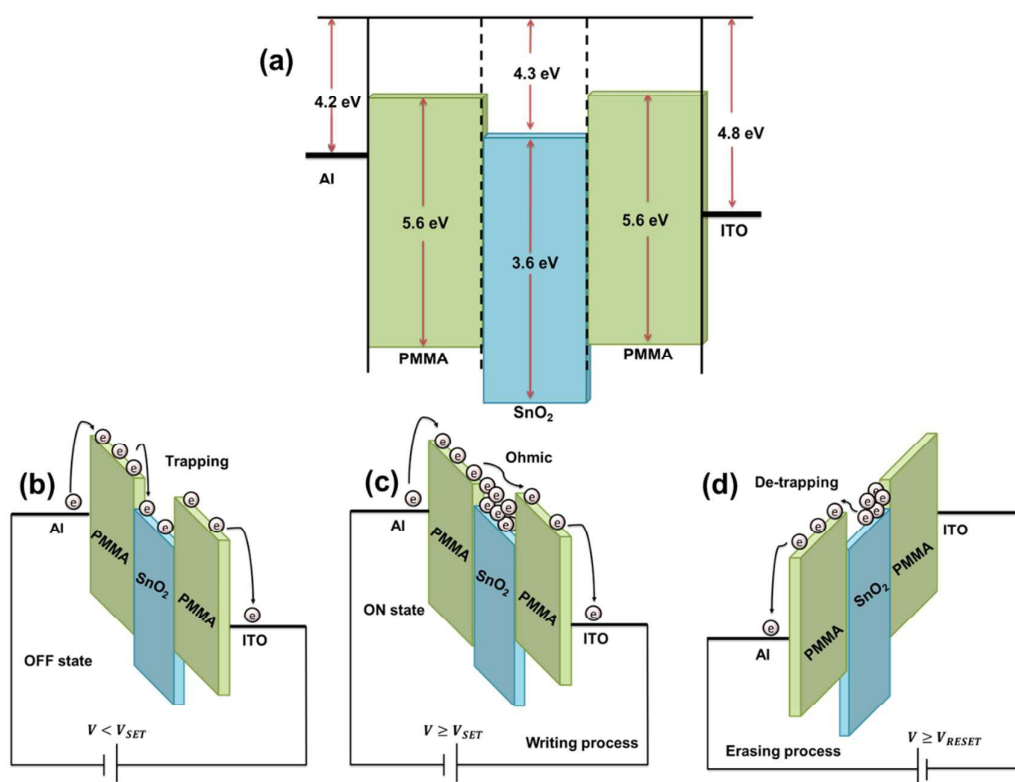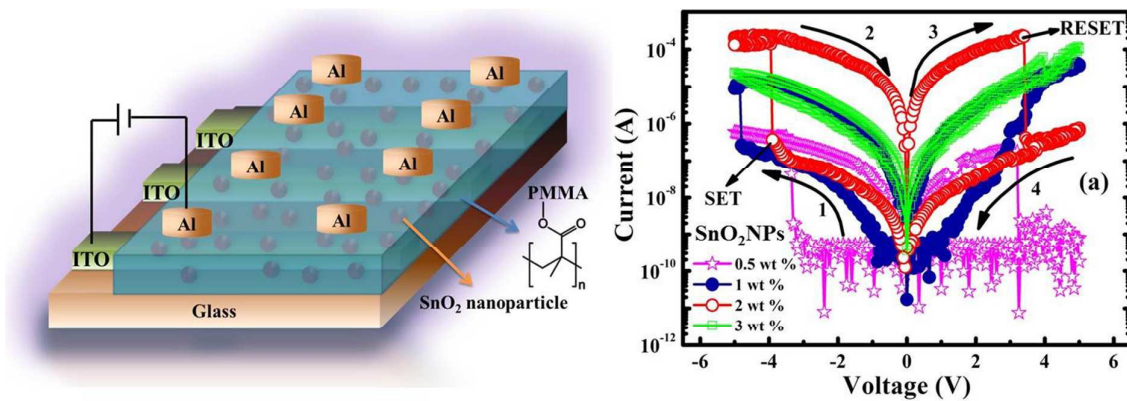P k Sarkar et al.

Figure 7

P k Sarkar et al.

Figure 8
P k Sarkar et al.

Graphical abstract

Various sizes of SnO$_2$ NPs have been successfully synthesized and embedded them into the insulating PMMA layer sandwiched between ITO and Al electrodes.

P K Sarkar et. al

1